PROCEEDINGS, 50th Workshop on Geothermal Reservoir Engineering
Stanford University, Stanford, California, February 10-12, 2025
SGP-TR-229

Modeling Hydraulic Fracture Opening and Closure with Proppant Transport and Settlement

Ming Yang[1], Travis McLing[1] and Wencheng Jin[1,2]

[1]Energy and Environmental Science and Technology Directorate, Idaho National Laboratory, Idaho Falls, Idaho, USA

[2]Harold Vance Department of Petroleum Engineering, Texas A&M University, College Station, Texas, USA

ming.yang@inl.gov, wencheng.jin@tamu.edu

Keywords: Hydraulic fracturing, proppant transport, fracture closure, penalty method, finite element

ABSTRACT

Hydraulic fracturing is a widely used reservoir stimulation technique for improving fluid circulation in rock formations with extremely low permeability, particularly in enhanced geothermal systems (EGS). To better understand the complex processes involved and improve hydraulic stimulation performance, we have developed ELK (ELectrical fracKing), a MOOSE-based 3D finite element application, to model the behavior of proppant-fluid mixtures in propagating fractures. ELK integrates both the fluid and proppant components, incorporating particle-driven processes such as gravity settling, particle-particle interactions, and strong density and viscosity contracts, in addition to conventional fluid-driven fracture propagation. In this contribution, we extend ELK to model propped fracture closure, which occurs after the injection phase due to a dramatic fluid pressure drop within the fracture plane. During the shut-in, flowback, and production periods, the fracture width decreases, with the closure behavior depending on proppant concentration. At low concentrations, closure follows a nonlinear joint law linked to the stiffness of asperities in the fracture walls. While at high concentrations, it is controlled by the properties of a packed proppant bed. The extended ELK application is validated against several benchmark examples, including normal separation of a bar, fracture opening and propagation in response to fluid injection, and a flowback analysis. We believe that ELK's enhanced capabilities can serve as a valuable tool for designing and optimizing EGS deployment.

1. INTRODUCTION

Hydraulic fracturing is a widely used reservoir stimulation technique that creates or enhances fractures and fracture networks in underground low-permeable rock formations. This process increases the reservoir permeability and facilitates fluid circulation. It has been applied in various geoscientific fields, including oil and gas extraction, enhanced geothermal systems, and in-situ mining. The hydraulic fracturing process involves injecting a high-pressure fluid mixture into the rock formation through a wellbore, which will initiate, enlarge, and propagate fractures in the rock. Upon the release of fluid pressure, the stimulated fracture may narrow or even close, reducing permeability and limiting fluid circulation. To prevent fracture closure, the injected fluid mixture typically contains fine suspending particles, known as proppants, which will flow with the fluid and settle within the fractures to maintain their aperture width. Therefore, understanding and modeling the interaction between fracture closure and proppant placement is crucial for improving hydraulic fracturing efficiency and maximizing production output.

Numerical modeling of hydraulic stimulation requires adequate consideration of fracture opening and proppant transport. Various computational approaches have been developed to simulate this behavior, which can generally be categorized into continuum-based and discontinuous methods. These approaches differ in how they treat the fracture path, either assuming it is known a priori or allowing it to evolve during the simulation (Chen et al. 2021). Common methods include the finite element method (FEM) and its specialized variants such as extended finite element (XFEM) (Mohammadnejad and Khoei 2013, Jin and Arson 2019), phase field modeling (PFM) (Costa et al. 2023), cohesive zone modeling (CZM) (Liu et al. 2023), or split node (Meng et al. 2023).

The inclusion of proppant transport during hydraulic stimulation introduces an additional layer of complexity, as it requires treating the fluid flow as a multiphase and/or multi-component problem involving two interpenetrating media (Barboza et al. 2021). To enhance computational efficiency, Eulerian-Eulerian numerical schemes are often employed, where both the fracturing fluid and proppant are treated as continua governed by mass conservation principles (Shiozawa and McClure 2016). Simulating slurry transport involves modeling it as a mixture flow with concentration-dependent fluid rheology (Kumar et al. 2019, Egert et al. 2023), while accounting for physical processes such as particle-particle interactions and gravity settling.

Although the simulation of hydraulic fracturing has been extensively studied, coupled simulations involving proppant transport remain relatively underexplored and numerically challenging. Wang (2020) developed a fully coupled numerical code that captures both hydraulic stimulation and proppant transport, including proppant bank formation. Hosseini and Khoei (2020) applied XFEM to simulate hydraulic fracturing with proppant transport and tip screen-out, while Zeng et al. (2019) coupled proppant transport to the analytical solution of the classical PKN model. Egert et al. (2025) implemented a weak coupling approach for proppant transport and hydraulic fracturing, interchanging information between the two simulations.

This study focuses on the fracture opening and closure behavior within a coupled simulation of hydraulic fracturing and proppant transport. The key aspect is the traction-separation law used to control crack initiation and propagation, where a residual aperture width is incorporated into a penalty term to prevent significant overlap in closed fractures. When coupled with proppant transport, we introduce

simple equations to correlate the residual aperture width with the proppant concertation. The validity of our approach is assessed through three benchmark examples, including (1) the normal separation of a bar, which evaluates the fundamental fracture opening and closure behavior; (2) a plane-strain KGD model, which tests the propagation and closure of a hydraulic fracture under controlled conditions; (3) a radial hydraulic fracture model with proppant transport, which examines the interaction between fracture growth and proppant placement. Together, these steps enhance our understanding of the complex interactions between hydraulic fracturing and proppant movement.

2. METHODS

The numerical modeling of hydraulic fracturing and proppant transport is performed using the finite element (FE) application ELK (ELectrical fracKing), which is built on the open-source MOOSE (Multiphysics Object-Oriented Simulation Environment) framework (Lindsay et al. 2022). The hydraulic fracturing component in ELK leverages MOOSE's solid mechanics and porous flow modules, incorporating a modified incomplete interior penalty Galerkin (IIPG) method (Liu et al. 2023) as discontinuous Galerkin (DG) kernels, with a linear extrinsic cohesive law applied. For proppant transport, the MOOSE porous flow module is extended in ELK to account for concentration-dependent fluid rheology. The coupling between these two components is achieved through the MOOSE MultiApp interface.

2.1 Hydraulic fracturing

The hydraulic fracturing component in ELK incorporates three coupled governing equations: the stress equilibrium equation for the porous bulk matrix, a Darcy-based flow equation for fluid flow within the porous bulk matrix, and an additional fluid flow equation for the flow within the fracture plane (Liu et al. 2020). The coupling effects considered include solid-fluid interaction within the porous media, the influence of aperture width on fluid flow and solid deformation near the fracture, fluid exchange between the fracture and the surrounding porous media, and the propagation of hydraulic fracture (Mohammadnejad and Khoei 2013). The primary variables include the solid displacement vector $\boldsymbol{u}$, the pore pressure for the fluid phase in the bulk matrix p, and the fluid pressure within the fracture plane p_a:

$$\nabla \cdot \boldsymbol{\sigma} + \boldsymbol{f} = \boldsymbol{0} \qquad \text{on } \Omega \backslash \Omega_a, \tag{1}$$

$$\alpha \dot{\varepsilon_v} + \frac{1}{M}\dot{p} + \nabla \cdot \boldsymbol{q} = s_q \qquad \text{on } \Omega \backslash \Omega_a, \tag{2}$$

$$\dot{w_a} + \frac{n}{K_f}\dot{p_a} + \nabla_a \cdot \boldsymbol{q}_a = s_a \qquad \text{on } S_a. \tag{3}$$

Here, Ω represents the entire domain, while $\Omega_a = w_a \times S_a$ denotes the set of all interior cracked sub-domains, with S_a as the intermediate fracture plane and w_a as the aperture width. $\boldsymbol{\sigma}$ is the Cauchy stress tensor, $\boldsymbol{q}$ is the flux within the porous media, and $\boldsymbol{q}_a$ is the flux within the fracture plane. The injection rates into the matrix and fracture are denoted by s_q and s_a, respectively. $\dot{\varepsilon_v}$ is the volumetric strain rate of the solid skeleton. The subscript a in equation (3) is specific to the fracture aperture, including the divergence operator ∇_a. Further details on the numerical implementation of these governing equations, based on the modified IIPG formulation (Liu et al. 2023), are presented and discussed in Liu et al. (2020) and Egert et al. (2025).

A traction-separation law (TSL) or cohesive zone model (CZM) is incorporated into equation (1) to describe the relation between the displacement jump ($\boldsymbol{\delta} = [\![\boldsymbol{u}]\!] = \boldsymbol{u}^+ - \boldsymbol{u}^-$) across the fracture plane and the traction $\boldsymbol{t}$, which governs crack initiation and propagation. This study adopts a linear extrinsic TSL based on Ortiz and Pandolfi (1999), where the relation between the effective traction t_{eff} and the effective displacement jump δ_{eff} is expressed as:

$$t_{\text{eff}} = \begin{cases} \left\langle 1 - \dfrac{\delta_{\text{eff}}}{\delta_c} \right\rangle t_c, & \text{if } \delta_{\text{eff}} = \delta_{\max} \text{ and } \dot{\delta} > 0 \\ \dfrac{t_{\max}}{\delta_{\max}} \delta_{\text{eff}}, & \text{otherwise} \end{cases} \tag{4}$$

Here, $\delta_{\text{eff}} = \sqrt{\beta^2 \|\boldsymbol{\delta}_s\|^2 + \langle \delta_n \rangle^2}$, where β is the ratio of the critical shear traction to the critical normal traction, with a typical value of 0.707. δ_n is the normal component of $\boldsymbol{\delta}$ relative to the fracture plane, while $\boldsymbol{\delta}_s$ is the shear component of $\boldsymbol{\delta}$ on the fracture plane. δ_c and t_c are two material model parameters, representing the characteristic displacement jump and traction, respectively. Similarly, the effective traction is given by $t_{\text{eff}} = \sqrt{\beta^{-2} \|\boldsymbol{t}_s\|^2 + \langle t_n \rangle^2}$. $\delta_{\max}$ is the maximum δ_{eff} reached during the loading history and serves as an internal variable to quantify loading or unloading. $t_{\max}$ is the traction corresponding to $\delta_{\max}$, and is computed as $\left\langle 1 - \frac{\delta_{\max}}{\delta_c} \right\rangle t_c$. The Macaulay brackets $\langle x \rangle$ are defined as $\langle x \rangle = 0$ if $x < 0$ and $\langle x \rangle = x$ if $x \geq 0$.

The conversion from t_{eff} to $\boldsymbol{t}$ is given by:

$$\boldsymbol{t} = \frac{t_{\text{eff}}}{\delta_{\text{eff}}} (\beta^2 \boldsymbol{\delta}_s + \delta_n \boldsymbol{n}) - \theta \langle -(\delta_n - \delta_{n,res}) \rangle^m \boldsymbol{n} \tag{5}$$

Equation (5) includes a penalty term $\theta \langle -(\delta_n - \delta_{n,res}) \rangle^m \boldsymbol{n}$ to prevent significant overlap once the fracture closes. Here θ is the penalty parameter used in the discontinuous Galerkin formulation (Liu et al. 2023), m is a model parameter that enhances numerical stability

(Bayat et al. 2020), and $\boldsymbol{n}$ is the normal vector to the fracture plane. $\delta_{n,res}$ represents the residual aperture width, which is zero by default but can be greater than zero when considering the contribution of proppant for preventing complete fracture closure.

It is important to note that before crack nucleation, $\boldsymbol{t} = \frac{1}{2}(\boldsymbol{\sigma}^{-} + \boldsymbol{\sigma}^{+}) \cdot \boldsymbol{n}$. Crack nucleation occurs when the computed t_{eff} exceeds t_c. Once crack nucleation happens, equations (3) and (4) are used to calculate the interface traction $\boldsymbol{t}$.

2.2 Proppant transport

To model the transport of proppants within the fracture, the aperture fluid is treated as a single-phase, two-component fluid consisting of water and proppant. The mass balance equations for each component are given by:

$$\frac{\partial n\rho_f(1-c)}{\partial t} + \nabla \cdot \left[n\rho_f(1-c)\boldsymbol{v}_f\right] = 0 \tag{6}$$

$$\frac{\partial n\rho_p c}{\partial t} + \nabla \cdot \left[n\rho_p c\boldsymbol{v}_p\right] = 0 \tag{7}$$

Here, n is the porosity, c is the proppant concentration, ρ_f and ρ_p are the densities of water and proppant, respectively, and $\boldsymbol{v}_f$ and $\boldsymbol{v}_p$ are the velocities of water and proppant. By introducing the average density and velocity of the water-proppant mixture, we obtain the mass balance equation by combining equations (6) and (7):

$$\frac{\partial n\rho_m}{\partial t} + \nabla \cdot [n\rho_m\boldsymbol{v}_m] = 0 \tag{8}$$

where $\rho_m = \rho_f(1-c) + \rho_p c$ and $\rho_m v_m = \rho_f(1-c)\boldsymbol{v}_f + \rho_p c\boldsymbol{v}_p$. The mixture (or slurry) velocity, $\boldsymbol{v}_m$ is assumed to be the Darcy's velocity, and is determined by

$$\boldsymbol{v}_m = -\frac{\kappa_f}{\mu_m}(\nabla p_a - \rho_m \boldsymbol{g}) \tag{9}$$

where p_a is the slurry pressure, μ_m is the slurry viscosity, and $\boldsymbol{g}$ is the gravity vector. The fracture permeability, κ_f, is dependent on the aperture width w_a and is given by $\kappa_f = \frac{w_a^2}{12}$.

With $\chi = \frac{\rho_p}{\rho_m}c$ the mass fraction of proppant, replacing c, and the slip velocity $\boldsymbol{v}_{\text{slip}} = \boldsymbol{v}_p - \boldsymbol{v}_f$, equations (6) and (7) can be reformulated as:

$$\frac{\partial n\rho_m(1-\chi)}{\partial t} + \nabla \cdot [n\rho_m(1-\chi)\boldsymbol{v}_m] - \nabla \cdot \left[n\rho_m(1-\chi)\chi\boldsymbol{v}_{\text{slip}}\right] = 0 \tag{10}$$

$$\frac{\partial n\rho_m\chi}{\partial t} + \nabla \cdot [n\rho_m\chi\boldsymbol{v}_m] + \nabla \cdot \left[n\rho_m(1-\chi)\chi\boldsymbol{v}_{\text{slip}}\right] = 0 \tag{11}$$

The slip velocity $\boldsymbol{v}_{\text{slip}}$ accounts for various effects that cause the particle velocity to deviate from the slurry velocity, such as gravitational particle settling, collisional effects, fluid-particle drag forces, and turbulent mixing. Further details, including empirical equations for particle-particle interactions, turbulent settling conditions, and concentration-dependent viscosity laws, can be found in Egert et al. (2025).

Equations (10) and (11), combined with equation (9) and the formulas for determining $\boldsymbol{v}_{\text{slip}}$, ρ_m, and μ_m, can be solved to determine the two primary variables p_a and χ. In ELK, these equations are solved using the Eulerian-Eulerian numerical scheme, which provides adequate accuracy given the small deformation within the fracture plane.

2.3 Coupling approach

The coupling approach between hydraulic fracturing (HF) and proppant transport (PT) used in this study relies on the MultiApp feature within the MOOSE framework. This feature enables multidimensional coupling in both fully coupled and loosely coupled manner, providing flexibility and efficiency in integrating different components of the simulation. Various types of physics can be solved independently in time and space, and then exchanged through spatial properties, variables, or shape functions. A main application (main app) coordinates the exchange between itself and the sub-applications, managing the overall coordination, convergence criteria and synchronization of the coupled simulation. A sub-app can be executed at any time during the main app solve, either loosely after each time step of the main app, or fully coupled through fixed-point iterations during the solve.

In this study, a loose coupling strategy is implemented, where the main application PT is solved after the sub-application HF completes its calculations. Time steps are synchronized between the two applications to ensure both are addressed in each time step. If an issue arises during the solution process, the time step is reduced, allowing the affected application to continue solving until it catches up. The mesh is shared between both applications, and nodal and elemental variables are used to transfer material properties between them. The sub-app solves for pressure and aperture, transferring these values to the main app. While pressure is defined across the entire domain, the aperture is confined to the fracture plane, often treated as an interface or lower-dimensional block. The aperture information in the main app is

then used to calculate the fracture permeability using the local cubic law (Witherspoon et al. 1980), with porosity as a scaling parameter to quantify lower-dimensional mass flow. PT calculates the proppant transport (restricted to the fracture plane) and updates concentration-dependent material parameters, such as fluid density and viscosity, which are then transferred back into the sub-app.

3. RESULTS

3.1 Bar failure

The effectiveness of the penalty method introduced in the traction-separation law in equation (5) is evaluated by simulating the response of a bar under stretching and compressing conditions. With Young's modulus of 100 MPa, the bar is initially stretched by displacing the top surface upward by 0.3 mm, then compressed by moving the top surface downward by 0.35 mm, and finally stretched again by 0.55 mm, as shown in Figure 1(a). Bar failure, marked by the activation of the extrinsic cohesive zone model, occurs during the initial stretching phase when the displacement reaches 0.1 mm, and the traction t exceeds $t_{\max}$ (=3 MPa), as seen in Figure 1(b).

In the subsequent loading stage, as the interface displacement jump δ increases, the numerical simulation closely matches the analytical solution derived from the cohesive zone model, as evidenced by the overlapping curves in Figure 1(c). During the unloading or second compression phase, as shown in Figure 1(c), the crack gap (or aperture width) nearly reaches $0.7\delta_c$ ($\delta_c = 0.4$ mm). Subsequently, the crack gap begins to reduce until it reaches the specified residual aperture width, $\delta_{n,res} = 0.1\delta_c$. If δ_n falls below $\delta_{n,\mathrm{res}}$, a substantial contact normal force is generated through the penalty term, preventing further reduction of δ_n. The inset in Figure 1(c) illustrates the gap between the top and bottom bar blocks, corresponding to the residual aperture width.

This simulation demonstrates the effectiveness of the penalty method in accurately modeling fracture closure behavior.

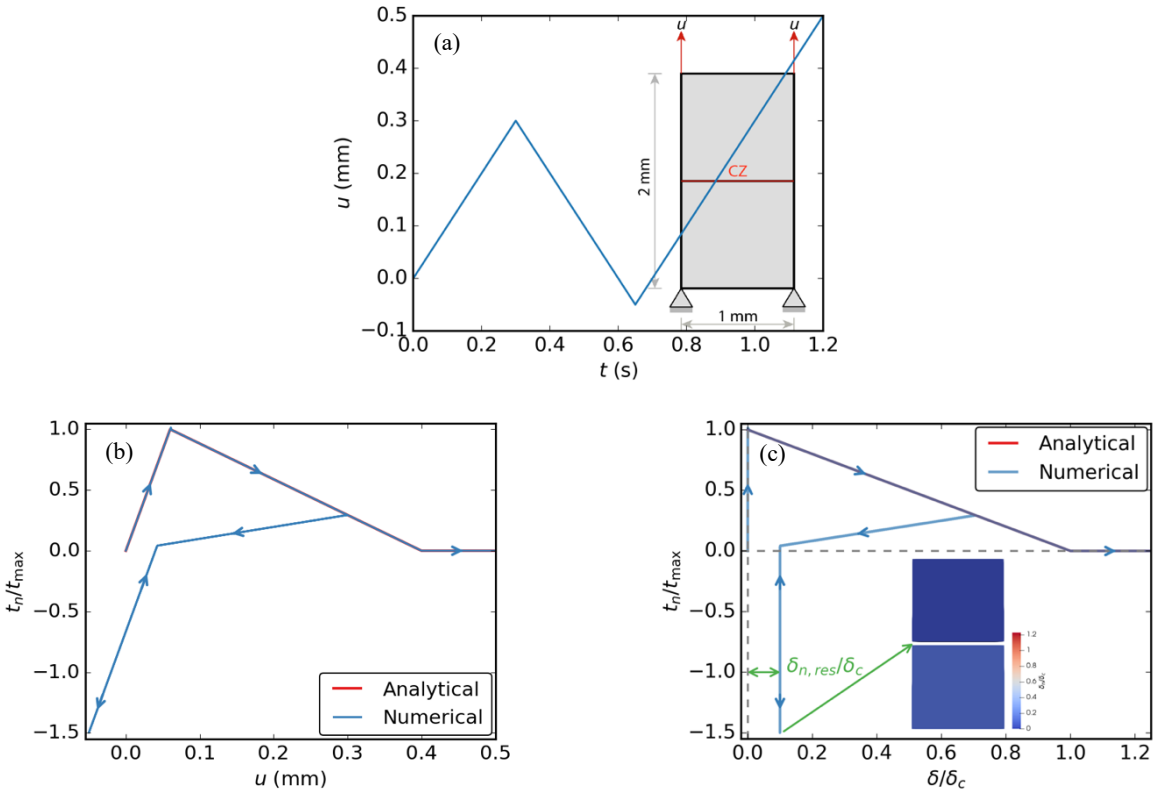

Figure 1: (a) Bar under normal separation during loading and unloading with contact included, (b) the relation between interface traction and displacement on the top of the bar, and (c) the relation between interface traction and interface displacement jump.

3.2 Plane-strain KGD model

To further evaluate the effectiveness of the penalty method in modeling fracture closure behavior, we simulate a plane-strain Kristianovich-Geertsma-de Klerk (KGD) hydraulic fracture. As illustrated in Figure 2(a), a 3D model with dimensions of 30 m × 60 m × 0.5 m is used to simulate the KGD hydraulic fracture, with a line source of injection deployed along the z axis. The model is fixed in the z direction, and the other boundary conditions are shown in Figure 2(a). The model parameters, detailed in Table 1, indicate that the hydraulic fracture propagates in a viscosity-dominated regime and can be approximated using the zero-toughness solution provided by Detournay (2004) during the injection phase.

The injection rate $Q_a = 0.001\ \mathrm{m}^2/\mathrm{s}$ is applied for the first 20 seconds to initiate and propagate the hydraulic fracture. Afterward, Q_a is set to $-0.0005\ \mathrm{m}^2/\mathrm{s}$ for 17 seconds to accelerate the fracture closure process ($\delta_{n,res} = 0$). Figure 2(b) shows the evolution of aperture width and pore pressure at the injection point. During the injection phase, the simulation results closely match the analytical solutions provided by Detournay (2004). Once the injection rate becomes negative, both aperture width and pore pressure decrease. The pore pressure becomes significantly negative before the fracture closes at 37 seconds.

Table 1: Model parameters for the plane-strain KGD and radial hydraulic fracture simulations

	Plane-strain KGD model	Radial hydraulic fracture model
Young's modulus, E (GPa)	38.8	17
Poisson's ratio, ν	0.15	0.2
Energy release rate, G_{IC} (N/m)	10	120
Tensile strength, t_c (MPa)	1	0.625
Fluid viscosity, μ_f (Pa s)	0.01	0.0001

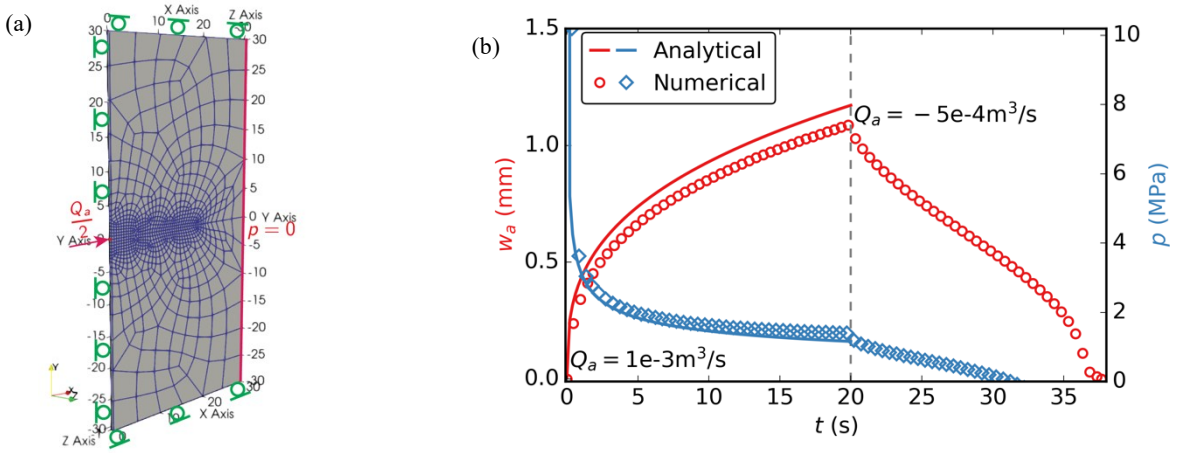

Figure 2: (a) Geometry of the Kristianovich-Geertsma-de Klerk (KGD) model in 3D (unit: m) and (b) evolution of aperture width and pore pressure at the injection point in viscosity-dominated regime.

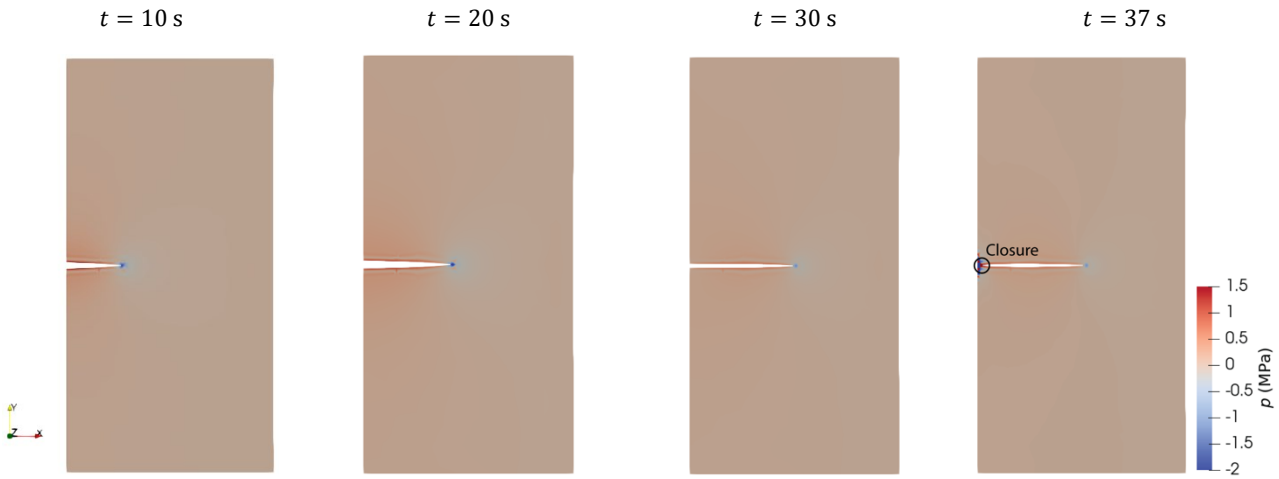

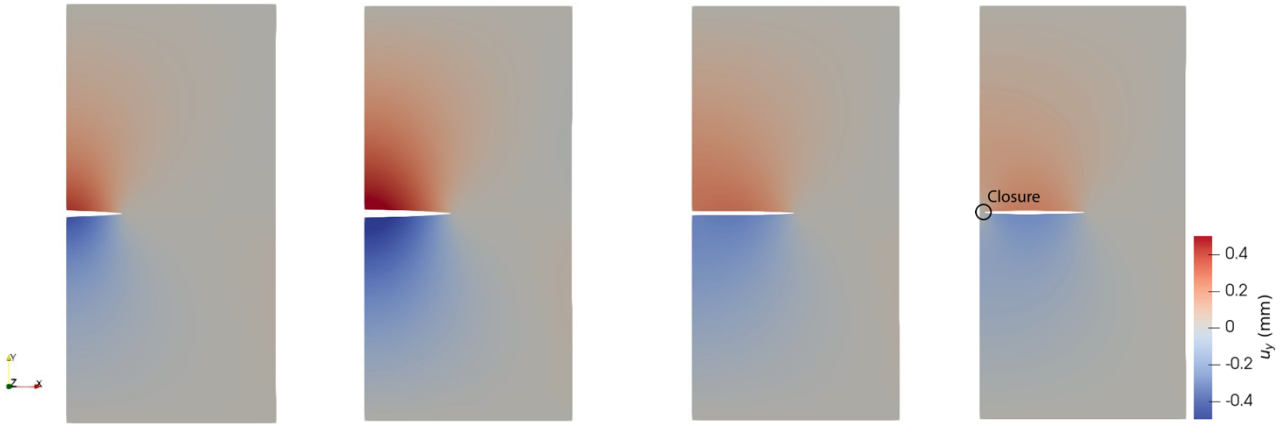

Figure 3: Distribution of pore pressure and displacement along y axis at the different snapshots of the simulation. The visual displacement of fracture surfaces is scaled by a factor 1000.

Figure 3 displays the distributions of pore pressure and displacement along y direction at the simulation time of 10 s, 20 s, 30 s, and 37 s. Notable observations include: (1) the fracture length continues to increase after the injection period, and (2) the fracture initially closes at the crack mouth with significant negative pore pressure. This mode of fracture mouth closure occurs due to the much higher production rate compared to the fluid transport rate (Taleghani et al. 2020). We also experimented with a less negative value of Q_a or replacing the injection with a constant pressure after the injection phase, which resulted in a more uniform fracture closure behavior. However, this approach requires significantly more simulation time to observe fracture closure, which is not presented here. It should be noted that our hydraulic fracturing model does not include the leak-off behavior, and as such, cannot capture the tip-receding closure where the leak-off dominates (Taleghani et al. 2020).

3.3 Radial hydraulic fracture model

Building on the work of Shiozawa and McClure (2016), we relate the residual aperture width $\delta_{n,res}$ to the normalized proppant concentration, $\bar{c} = c/c_{\max}$, where c and $c_{\max}$ are the current and maximum proppant concentrations, respectively. The residual aperture width is determined as follows:

- $\delta_{n,\mathrm{res}} = 0$ when $\bar{c}\delta_n$ is less than the proppant size d_p,
- $\delta_{n,\mathrm{res}} = \bar{c}\delta_n$ when $\bar{c}\delta_n > d_p$ and $\bar{c} < 0.95$,
- $\delta_{n,\mathrm{res}} = \max(\delta_{n,\mathrm{res}}(t-\Delta t), \bar{c}\delta_n)$ when $\bar{c}\delta_n > d_p$ and $\bar{c} \geq 0.95$,

where $\delta_{n,\mathrm{res}}(t-\Delta t)$ is the residual aperture width from the previous time step.

To assess the effectiveness of this approach, we simulate a radial hydraulic fracture model. The simulation considers a penny-shaped hydraulic fracture propagating within an infinite linear elastic medium subjected to confining stress, as illustrated in Figure 4. The model dimensions are $8\mathrm{m} \times 16\mathrm{m} \times 16\mathrm{m}$, with a planar fracture positioned in x-z plane at the center of the model, as depicted in Figure 4(b). The model parameters are provided in Table 1.

An extrinsic traction-separation law is assigned to the interface elements on the fracture plane when the traction exceeds $t_{\max}$. Fluid is injected with a proppant concentration of 0.07 as a Dirac source at the origin, using a flux of 1 kg/s for 15 seconds to initiate and propagate the hydraulic fracture. Afterward, the flux is set to zero, and the simulation continues for an additional 100 seconds to observe fracture closure.

During the injection phase, the fracture is expected to nucleate and propagate while the aperture width reduces following the cessation of fluid injection. Roller boundary conditions are applied to all boundaries, allowing displacements parallel to the boundary plane but constraining movement in the normal direction. The top ($z = 8$ m) and bottom ($z = -8$ m) boundaries maintain a constant pressure defined by the function $\rho_f g(8 - z)$, where ρ_f is the fluid density ($1000\ \mathrm{kg/m^3}$) and g is the gravity ($9.81\ \mathrm{m/s^2}$).

Figure 5 depicts the distributions of aperture width and normalized proppant concentration at the end of the fluid injection (time=15s). The results clearly show the radial evolution of the fracture around the injection point, with the proppant concentrating near the crack tip.

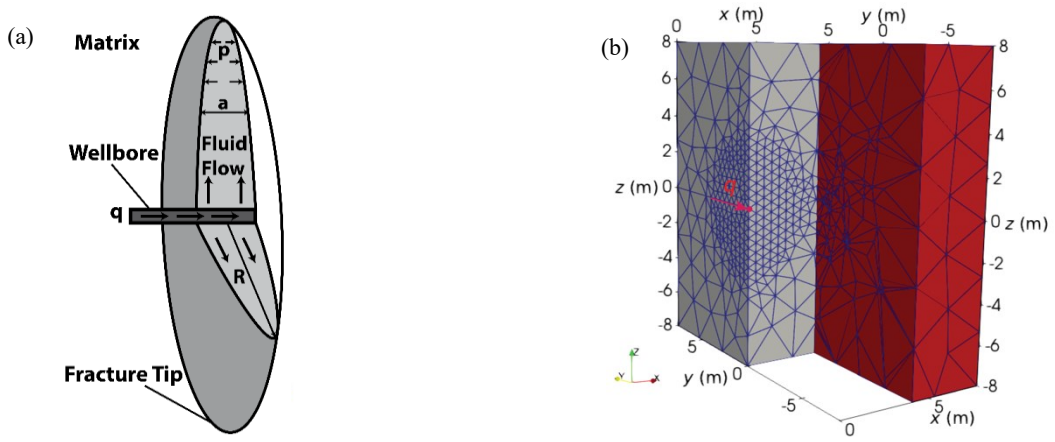

Figure 4: (a) Sketch of a penny-shaped hydraulic fracture model and (b) the mesh used for simulation. One-quarter of the mesh is omitted to show the fracture in the *x*-*z* plane.

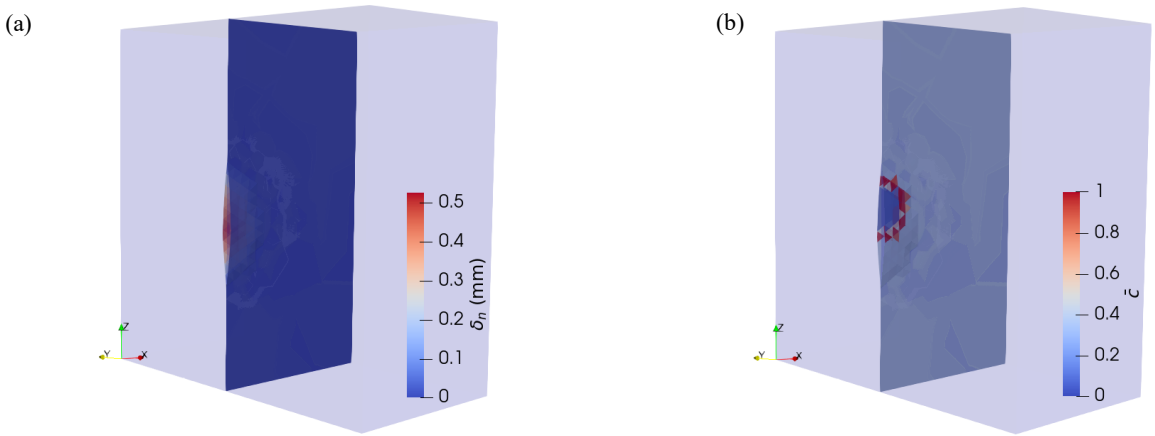

Figure 5: Distributions of aperture width δ_n and normalized proppant concentration $\bar{c}$ at the end of the injection phase. The visual displacement of both fracture surfaces is scaled by a factor 1000.

To better demonstrate the impact of fracture closure behavior, we conduct two simulations that differ only in whether the computed residual aperture width $\delta_{n,\mathrm{res}}$ is incorporated into the traction-separation law. Figure 6 compares the results from these simulations, illustrating the aperture width distribution at the end of fluid injection (time=15 s) and at the conclusion of the simulation (time=115 s).

In the first simulation, shown in Figure 6 (a) and (c), the residual crack gap in the traction-separation law is set to zero, effectively ignoring the computed $\delta_{n,\mathrm{res}}$. In the second simulation, depicted in Figure 6 (b) and (d), the residual crack gap is assigned the calculated $\delta_{n,\mathrm{res}}$. Interestingly and surprisingly, this difference influences the results even during the fluid injection phase, as evident from the differences between Figure 6 (a) and (b). For both cases, it is reasonable to observe that $\delta_{n,\mathrm{res}} \leq \delta_n$.

However, the differences become more pronounced by the time of 115 s, as seen when comparing Figure 6 (c) and (d). With a zero residual crack gap, Figure 6 (c) shows a significantly smaller aperture width compared to Figure 6 (d). It is worth noting that Figure 6 (d) shows δ_n falls slightly below $\delta_{n,\mathrm{res}}$ in certain regions, which is consistent with the penalty method allowing small contact overlaps.

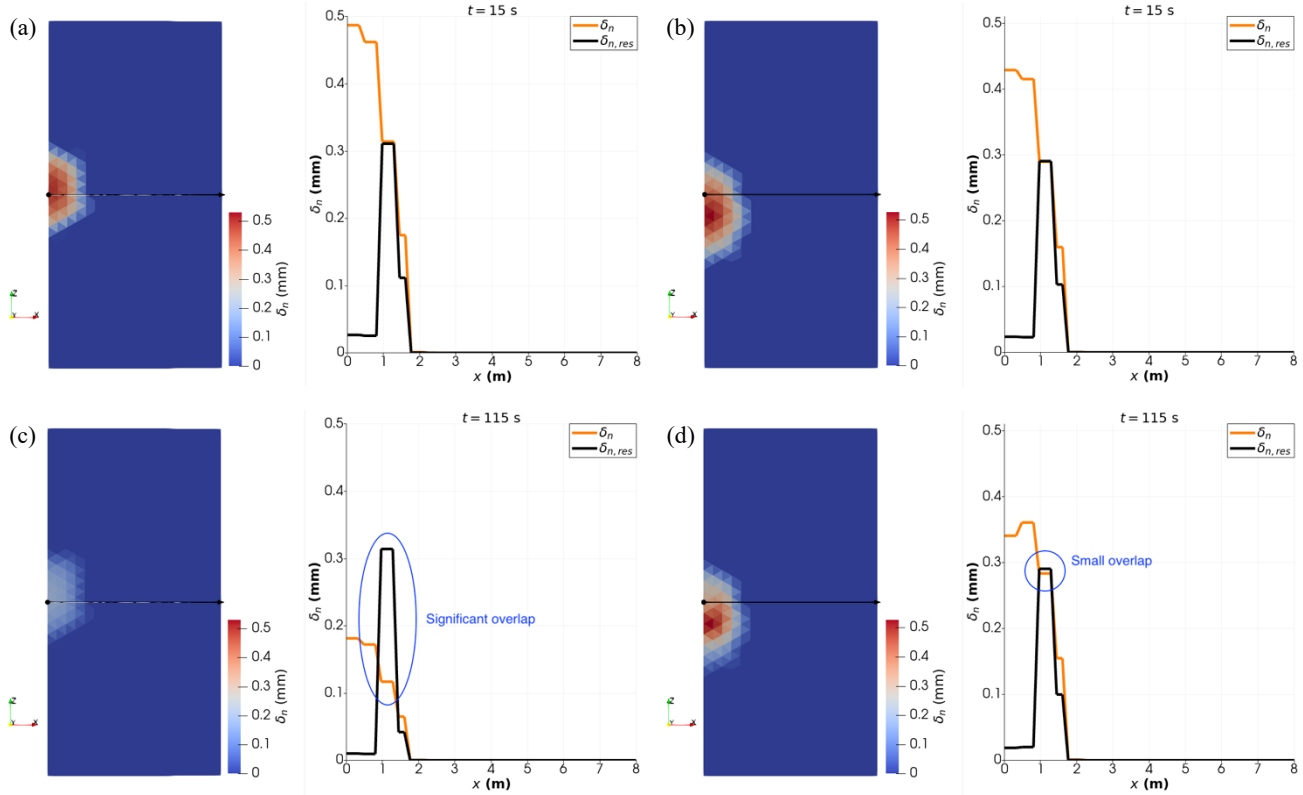

Figure 6: aperture width distribution in the fracture plane at the time of (a) 15 s and (c) 115s for the simulation with a zero $\delta_{n,res}$ assigned to the traction-separation law; aperture width distribution in the fracture plane at the time of (b) 15 s and (d) 115s for the simulation with the computed $\delta_{n,res}$ assigned to the traction-separation law. The curves in the plots refer to the values of δ_n or $\delta_{n,res}$ along the x axis.

4. CONCLUSIONS

This study extends the capabilities of the existing ELK code, originally developed for coupled simulations of hydraulic fracturing and proppant transport, by incorporating a model for fracture closure behavior. A key feature of this extension is the introduction of the residual aperture width, which governs the degree of fracture closure. This term plays a crucial role in the penalty component of the traction-separation law, ensuring that significant overlap is prevented once the fracture begins to close. Moreover, in the context of proppant transport, the residual aperture width is assumed to be a function of proppant concentration, which is modeled through three simple yet effective equations. The validity of this approach is demonstrated through three benchmark cases of increasing complexity, each designed to test different aspects of fracture behavior and proppant dynamics. While the results show promising accuracy, further studies are required to quantitatively validate this approach under more varied and realistic conditions.

ACKNOWLEDGEMENT

The information, data, or work presented herein was funded in part by the Advanced Research Projects Agency-Energy (ARPA-E), U.S. Department of Energy (DOE), under Award Number DE-AR0001709. Any opinions, findings and conclusions, or recommendations expressed in this material are those of the authors and do not necessarily reflect those of the DOE or the U.S. Government.

REFERENCES

Barboza, B. R., Chen, B. and Li, C.: A review on proppant transport modelling, Journal of Petroleum Science and Engineering, 204, (2021).

Bayat, H.R., Rezaei, S., Brepols, T. and Reese, S.: Locking-free interface failure modeling by a cohesive discontinuous Galerkin method for matching and nonmatching meshes, International Journal for Numerical Methods in Engineering, 121, 8, (2020), 1762-1790.

Chen, B., Barboza, B. R., Sun, Y., Bai, J., Thomas, H. R., Dutko, M., Cottrell, M. and Li, C.: A Review of Hydraulic Fracturing Simulation, Archives of Computational Methods in Engineering, 29, 4, (2021), 1-58.

Costa, A., Hu, T. and Dolbow, J. E.: On formulations for modeling pressurized cracks within phase-field methods for fracture, Theoretical and Applied Fracture Mechanics, 127, (2023).

Dahi Taleghani, A., Cai, Y. and Pouya, A.: Fracture closure modes during flowback from hydraulic fractures. International Journal for Numerical and Analytical Methods in Geomechanics, 44, 12, (2020), 1695-1704.

Detournay, E.: Propagation regimes of fluid-driven fractures in impermeable rocks. International Journal of Geomechanics, 4, 1, (2004), 35-45.

Egert, R., Gholami Korzani, M., Held, S. and Kohl, T.: Thermo-hydraulic Modeling of an Enhanced Geothermal System in the Upper Rhine Graben using MOOSE/TIGER, Proceedings WGC2020+1, Reykjavik, (2021).

Egert, R., Fournier, A. and Jin, W.: Modeling proppant transport and settling in 3D propagating fracture, Submitted, (2025).

Egert, R.W., Jin, W., Fournier, A. and Meng, C.: A Novel Workflow for Coupled Simulation of Hydraulic Stimulation with Simultaneous Injection of Proppant, 49th Workshop on Geothermal Reservoir Engineering, (2024), 1-11.

Gao, Q. and Ghassemi, A.: Finite element simulations of 3D planar hydraulic fracture propagation using a coupled hydro-mechanical interface element. International Journal for Numerical and Analytical Methods in Geomechanics, 44, 15, (2020), 1999-2024.

Hosseini, N. and Khoei, A. R.: Numerical simulation of proppant transport and tip screen-out in hydraulic fracturing with the extended finite element method, International Journal of Rock Mechanics and Mining Sciences, 128, (2020).

Jin, W. and Arson, C.: Fluid-driven transition from damage to fracture in anisotropic porous media: a multi-scale XFEM approach, Acta Geotechnica, 15, 1, (2019), 113-144.

Kumar, D., Gonzales, R. and Ghassemi, A.: The Role of Micro-Proppants in Conductive Fracture Network Development, SPE Hydraulic Fracturing Technology Conference and Exhibition, The Woodlands, (2019).

Lindsay, A. D., Gaston, D. R., Permann, C. J., Miller, J. M., Andrs, D., Slaughter, A. E., Kong, F. D., Hansel, J., Carlsen, R. W., Icenhour, C., Harbour, L., Giudicelli, G. L., Stogner, R. H., German, P., Badger, J., Biswas, S., Chapuis, L., Green, C. P., Hales, J., Hu, T. C., Jiang, W., Jung, Y. S., Matthews, C., Miao, Y. B., Novak, A., Peterson, J. W., Prince, Z. M., Rovinelli, A., Schunert, S., Schwen, D., Spencer, B. W., Veeraraghavan, S., Recuero, A., Yushu, D., Wang, Y. Q., Wilkins, A. and Wong, C. S. P.: 2.0-MOOSE: Enabling massively parallel multiphysics simulation, Softwarex, 20, (2022).

Liu, R., Jin, W., Harbour, L., Kong, F., Permann, C., Gaston, D. and Podgorney, R.: A robust interface finite element formulation for modeling brittle material failure problems, International Journal for Numerical Methods in Engineering, 124, 23, (2023), 5356-5374.

Liu, R., Liu, Z. and Wheeler, M.F.: A DG-based interface element method for modeling hydraulic fracturing in porous media, Computer Methods in Applied Mechanics and Engineering, 370, (2020), 113284.

Meng, C., Fournier, A. and Jin, W.: A Split-node Method for Modeling Pulse and Hydraulic Fracturing, ARMA Symposium, Atlanta, (2023).

Mohammadnejad, T. and Khoei, A.R.: An extended finite element method for hydraulic fracture propagation in deformable porous media with the cohesive crack model, Finite Elements in Analysis and Design, 73, (2013), 77-95.

Ortiz, M. and Pandolfi, A.: Finite-deformation irreversible cohesive elements for three-dimensional crack-propagation analysis, International journal for numerical methods in engineering, 44, 9, (1999), 1267-1282.

Shiozawa, S. and McClure, M.: Simulation of proppant transport with gravitational settling and fracture closure in a three-dimensional hydraulic fracturing simulator, Journal of Petroleum Science and Engineering, 138, (2016), 298-314.

Wang, J.: Propagation, proppant transport, and the evolution of transport properties of fluid-driven fractures, PhD, Pennsylvania State University, (2020).

Witherspoon, P. A., Wang, J. S. Y., Iwai, K. and Gale, J. E.: Validity of Cubic Law for fluid flow in a deformable rock fracture, Water Resources Research, 16, 6, (1980), 1016-1024.

Zeng, J., Li, H. and Zhang, D.: Numerical simulation of proppant transport in propagating fractures with the multi-phase particle-in-cell method, Fuel, 245, (2019), 316-335.